Energy 64 (2014) 287–297

Contents lists available at ScienceDirect

Energy

journal homepage: www.elsevier.com/locate/energy

# Modeling and simulation for the design of thermal-concentrated solar thermoelectric generator

Wei-Hsin Chen [a,*], Chien-Chang Wang [b], Chen-I Hung [b], Chang-Chung Yang [c], Rei-Cheng Juang [c]

[a] Department of Aeronautics and Astronautics, National Cheng Kung University, Tainan 701, Taiwan, ROC
[b] Department of Mechanical Engineering, National Cheng Kung University, Tainan 701, Taiwan, ROC
[c] Green Energy and Environmental Laboratories, Industrial Technology Research Institute, Hsinchu 300, Taiwan, ROC

ARTICLE INFO

*Article history:*
Received 17 April 2013
Received in revised form
23 September 2013
Accepted 23 October 2013
Available online 21 November 2013

*Keywords:*
Thermal-concentrated solar thermoelectric generator
Thermal concentration ratio
Numerical simulation
Equivalent model
Finite element scheme
Water cooling

ABSTRACT

The performances of thermal-concentrated solar thermoelectric generators (TEGs) at three different geometric types are investigated numerically to aid in designing practical devices. The temperature-dependent properties of the commercial thermoelectric material are taken into account, and an equivalent model based on the three-dimensional finite element scheme is developed to simplify and accelerate simulations. The constriction thermal resistance and thermal spreading resistance are considered in the equivalent model. Increasing substrate area increases the thermal concentration ratio; this improves the performance of the solar TEG. In the three geometric types, the smallest element with the substrate area of $90 \times 90$ mm$^2$ provides the maximum system efficiency of 4.15%. For a TEG at a given element length, decreasing the cross-sectional area of the thermoelectric element is a feasible route to improve the performance. Under the situation of forced convection, varying convection heat transfer coefficient has an ignorable effect on the performance. For equal convective heat transfer coefficients, water cooling is better than air cooling for the net output power of the TEG because of its increased specific heat. Therefore, water cooling is recommended for the cooling of the solar TEG.

© 2013 Elsevier Ltd. All rights reserved.

## 1. Introduction

Thermoelectric generators (TEGs) are energy conversion devices, which unlike convectional heat engines, are entirely solid-state, environmentally friendly, extremely reliable, simple, compact, and safe [1,2]. When a temperature difference across a TEG exists, it will generate electrical power through the Seebeck effect [3,4]. Although the principle of thermoelectricity was discovered in 1834, there were few practical applications until the middle 1950s [5]. Since the first and the second energy crises occurred in the 1970s, considerable interest has arisen in the development of thermoelectric power generation [6]. The applications of TEGs are limited due to their relatively low conversion efficiency [7,8]. Waste heat is extensively encountered in many industrial and manufacturing processes [9,10] and it is low-cost and even no-cost if waste heat can be recovered. Therefore, the low efficiency problem of TEGs is not a critical issue when they are applied in such settings [7] if waste heat is used as the heat source of the TEG. Moreover, the energy conversion process of TEGs is totally green [11] so that they are able to abate greenhouse gas emissions.

A number of practical applications of thermoelectric devices through waste heat recovery can be found in literature. Hsiao et al. [12] proposed a theoretical model to predict the performance of a TEG module by recovering waste heat from an automobile engine. Their results showed that the performance of the TEG installed on an exhaust pipe was better than that installed on a radiator. Hsu et al. [13] constructed a thermoelectric system, which comprised 24 TEG modules to recover waste heat from the exhaust pipe of an automobile, to find its optimum operating conditions. Chen et al. [14] investigated the characteristics of thermoelectric modules used for power generation by recovering low-temperature waste heat at various operating conditions. They discovered that the effects of the flow pattern of the heat sink and the water flow rate on the performance of the modules were not significant, whereas the heat source or the heating temperature played an important role on the performance.

Another low-cost heat source is the solar energy which has been widely applied in industries, such as solar thermal systems and photovoltaic systems [15]. In recent years, solar-driven TEGs have received a great deal of attention and a lot of studies have been carried out. One of the common designs of solar thermoelectric

* Corresponding author. Tel.: +886 6 2004456; fax: +886 6 2389940.
*E-mail address:* weihsinchen@gmail.com (W.-H. Chen).

0360-5442/$ – see front matter © 2013 Elsevier Ltd. All rights reserved.
http://dx.doi.org/10.1016/j.energy.2013.10.073

**Nomenclature**

| | |
|---|---|
| $A_c$ | cross-sectional area of the collector ($mm^2$) |
| $C_p$ | specific heat at constant pressure ($kJ\ kg^{-1}\ K^{-1}$) |
| $C_{opt}$ | optical concentration ratio of solar thermoelectric generator |
| $C_{th}$ | thermal concentration ratio of solar thermoelectric generator |
| $D$ | depth of thermoelectric element (mm) |
| $D_g$ | fin-to-fin spacing (mm) |
| $\vec{E}$ | electric field intensity vector ($V\ m^{-1}$) |
| $F$ | area factor |
| $G$ | curve fitting functions of relative error |
| $H_f$ | fin height (mm) |
| $h_L$ | convection heat transfer coefficient at the TEG's cold side ($W\ m^{-2}\ K^{-1}$) |
| $I^L$ | electric current load vector (A) |
| $\vec{J}$ | electric current density vector ($A\ m^{-2}$) |
| $K^{TT}$ | thermal stiffness matrix |
| $K^{\varphi T}$ | Seebeck stiffness matrix |
| $K^{\varphi\varphi}$ | electric stiffness matrix |
| $k$ | thermal conductivity ($W\ m^{-1}\ K^{-1}$) |
| $L$ | length of thermoelectric element (mm) |
| $L_{HS}$ | length of heat sink (mm) |
| $\dot{m}$ | mass flow rate of fluid ($kg\ s^{-1}$) |
| $m$ | constant for the curve fitting function |
| $N$ | element shape function |
| $n_f$ | number of fins |
| $n$ | constant for the curve fitting function |
| $P_{equivalent}$ | output power of equivalent model (W) |
| $P_{out}$ | output power (W) |
| $P_{pump}$ | pumping power (mW) |
| $P_{real}$ | output power of real model (W) |
| $q_s$ | solar irradiance ($W\ m^{-2}$) |
| $Q$ | heat transfer rate (W) |
| $Q_H$ | heat transfer rate at the solar TEG's hot side (W) |
| $Q_{in}$ | input energy of solar thermoelectric generator (W) |
| $Q_L$ | heat transfer rate at the solar TEG's cold side (W) |
| $Q^L$ | thermal load vector (W) |
| $T$ | temperature (°C) |
| $T_e$ | vector of nodal temperatures (°C) |
| $T_f$ | surface temperature of fins (°C) |
| $t_f$ | fin thickness (mm) |
| $T_\infty$ | environment temperature (°C) |
| $U$ | mean velocity of fluid ($m\ s^{-1}$) |
| $W$ | width of thermoelectric element (mm) |
| $W_{HS}$ | width of heat sink (mm) |

*Greek letters*

| | |
|---|---|
| $\alpha$ | Seebeck coefficient ($V\ K^{-1}$) |
| $\gamma$ | electrical conductivity ($S\ m^{-1}$) |
| $\varepsilon$ | emissivity of the solar absorber |
| $\eta_a$ | absorptivity of the collector coating |
| $\eta_{opt}$ | optical efficiency of the Fresnel lens |
| $\eta_T$ | total efficiency of the system |
| $\eta_{TEG}$ | conversion efficiency of the TEG |
| $\mu$ | fluid viscosity ($N\ s\ m^{-2}$) |
| $\rho$ | fluid density ($kg\ m^{-3}$) |
| $\rho_e$ | electrical resistivity (Ω m) |
| $\sigma^2$ | coefficient of determination |
| $\sigma_{SB}$ | Stefan–Boltzmann constant ($= 5.67 \times 10^{-8}\ W\ m^{-2}\ K^{-4}$) |
| $\phi$ | electric scalar potential (V) |
| $\varphi_e$ | vector of nodal electric potentials (V) |
| $\Delta p$ | pressure drop across the heat sink ($N\ m^{-2}$) |

*Subscripts*

| | |
|---|---|
| a | air |
| f | fin |
| H | hot side |
| HS | heat sink |
| L | cold side |
| rd | radiation |
| w | water |

systems is the optical-concentrated solar TEG which uses an optical concentration system to focus sunlight on the hot side of the TEG. Li et al. [16] designed a prototype optical-concentrated solar TEG and used a numerical method to evaluate its performance. Their results showed that the efficiency of the TEG could reach up to 9.8, 13.5, and 14.1% when $Bi_2Te_3$, skutterudite, and LAST alloys were employed as the materials of the TEG, respectively. Fan et al. [17] fabricated and experimentally tested an optical-concentrated solar TEG system along with a parabolic dish concentrator. The system was able to produce electric power up to 5.9 W under the temperature difference of 35 °C with the hot-side temperature of 68 °C. Yang et al. [18] developed a numerical model to analyze the performance of a TEG module with optical concentration. Their results suggested that the efficiency of the TEG decreased to 3.85% and had a relative drop of 61.3% when the contact resistance and all heat losses were considered. Xiao et al. [19] analyzed the performance of a multi-stage solar TEG by means of a numerical method. They pointed out that that the efficiency of the solar TEG system could reach 10.52% based on a three-stage thermoelectric module.

As far as the thermal-concentrated solar TEG is concerned, a flat-panel solar absorber on the hot side of the TEG is used to concentrate the solar heat through heat conduction. Kraemer et al. [20] designed a flat-panel solar TEG system with high thermal concentration; the system with the conditions of a thermal concentration ratio of 299 and AM1.5G (1 $kW\ m^{-2}$) could attain a peak efficiency of 4.6%. Chen [21] developed a theoretical model to evaluate the efficiency of a TEG pair in association with thermal concentration and optical concentration. His results suggested that the efficiency of the TEG pair under thermal concentration but with little or no optical concentration could be larger than 5% when the hot-side temperature was between 150 and 250 °C.

According to the above literature review, the two routes of optical concentration and thermal concentration can be utilized to improve the performance of solar TEGs. The optical concentrator is generally costly [22]. On the other hand, very little research has been performed on the thermal-concentrated solar TEG, especially in numerical simulation. For this reason, the objective of this study is to numerically investigate the performance of a solar TEG with thermal concentration. A three-dimensional finite element scheme will be employed to model the TEG system. In some studies [12,13,21], the properties of thermoelectric materials were assumed to be constant. This may induce a numerical deviation at high temperatures. Consequently, the temperature-dependent properties of the thermoelectric materials are considered in this work. In particular, an equivalent model is developed to simplify and accelerate the numerical approach. The effects of substrate area and thermoelectric element geometry on the performance of the TEG will be explored. Eventually, the power consumption for the cooling of the TEG is predicted via a theoretical method to evaluate the net output power of the TEG system.

## 2. Methodology

### 2.1. Physical model and assumptions

The schematic of the investigated thermal-concentrated solar TEG system is shown in Fig. 1a. In the system, a solar absorber with the heat uptake of $Q_H$ is located at the hot side of the TEG. Meanwhile, the heat $Q_L$ is liberated to the heat sink at the cold side of the TEG. The generated electrical current is used to power the external loading. Fig. 1b demonstrates the practical unpackaged thermoelectric module with the size of 100 × 100 mm, which contains 16 thermoelectric (TE) pairs. The commercial bismuth telluride elements were purchased from a company in Taiwan (Tande Energy and Temperature Associates PTY. CO.). Prior to performing simulations, the following assumptions are adopted to simplify the problem.

(1) The solar TEG is in steady-state.
(2) The configurations of the p-type and n-type elements are identical.
(3) The thermoelectric elements are connected electrically in series and thermally in parallel.
(4) The material properties of the thermoelectric elements are temperature-dependent, but the material properties of the solar absorber, substrate, and electrode are constants.
(5) The whole system is in a vacuum environment [20,21], so the heat loss due to heat convection is neglected.
(6) The radiation heat transfer only exists between the hot-side surface and the environment.
(7) The solar absorber and the heat sink are not included in the computational domain, but their behavior is described by boundary conditions.

Based on the preceding assumptions, only one thermoelectric pair, including a p-type element and an n-type element, is considered in the computational domain, as shown in Fig. 2a. The substrate area for thermal concentration is usually much larger than the cross-sectional area of the elements. For example, when 16 TE pairs are included in a solar TEG module with the substrate area of 100 × 100 mm$^2$, the average substrate area for each TE pair is 25 × 25 mm$^2$, whereas the cross-sectional area of the TE element is 1 × 1 mm$^2$, as shown in Fig. 2b. The thermal concentration is characterized by the thermal concentration ratio ($C_{th}$) which is defined as the area ratio of the solar absorber to the cross-sectional area of the thermoelectric elements [20,21]. Therefore, the value of $C_{th}$ in Fig. 2b is 312.5. In the real model, the substrate area is given in accordance with a realistic geometry. In the equivalent model, however, the substrate area is assumed to be identical to the given element geometry, and an area factor is embedded in the boundary conditions to approach the input energy, dissipated energy, and the radiation heat which are equal to those of the real model. The advantage of the equivalent model is that the number of computational cells can be minimized so as to reduce the computational time significantly when compared to the real model.

### 2.2. Governing equations

The behavior of a thermoelectric material is described by the following governing equations which couple the thermal and electrical fields [23,24]:

$$\nabla\cdot\left(\alpha T\vec{J}\right) - \nabla\cdot(k\nabla T) = \vec{J}\cdot\vec{E} \tag{1}$$

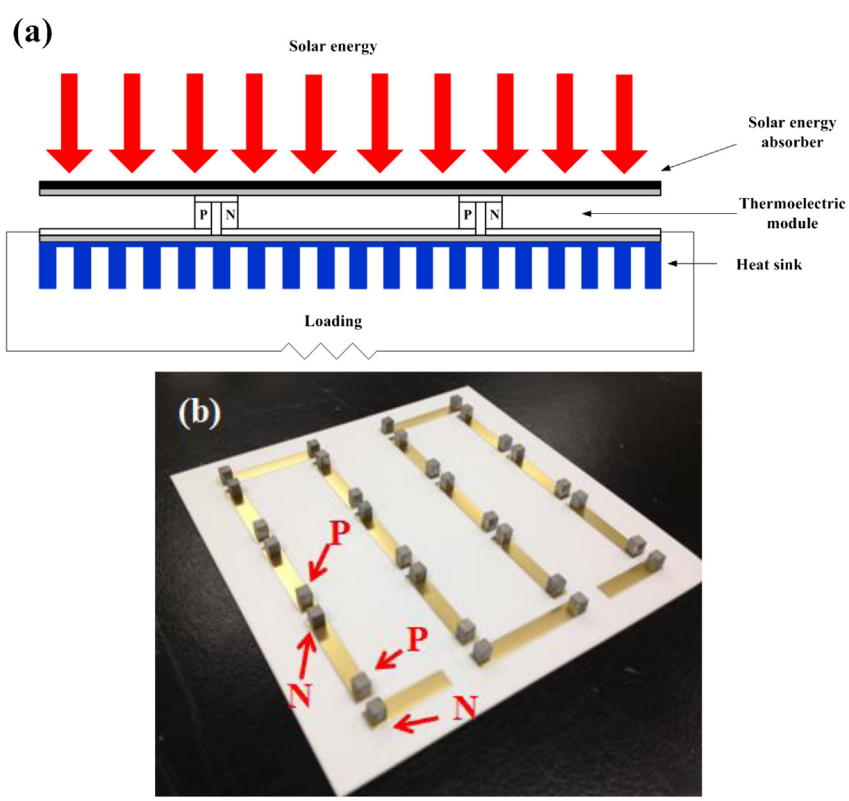


**Fig. 1.** (a) Schematic of thermal-concentrated solar TEG system and (b) photograph of the unpackaged thermoelectric module (P and N represents the p-type and n-type thermoelectric elements, respectively).

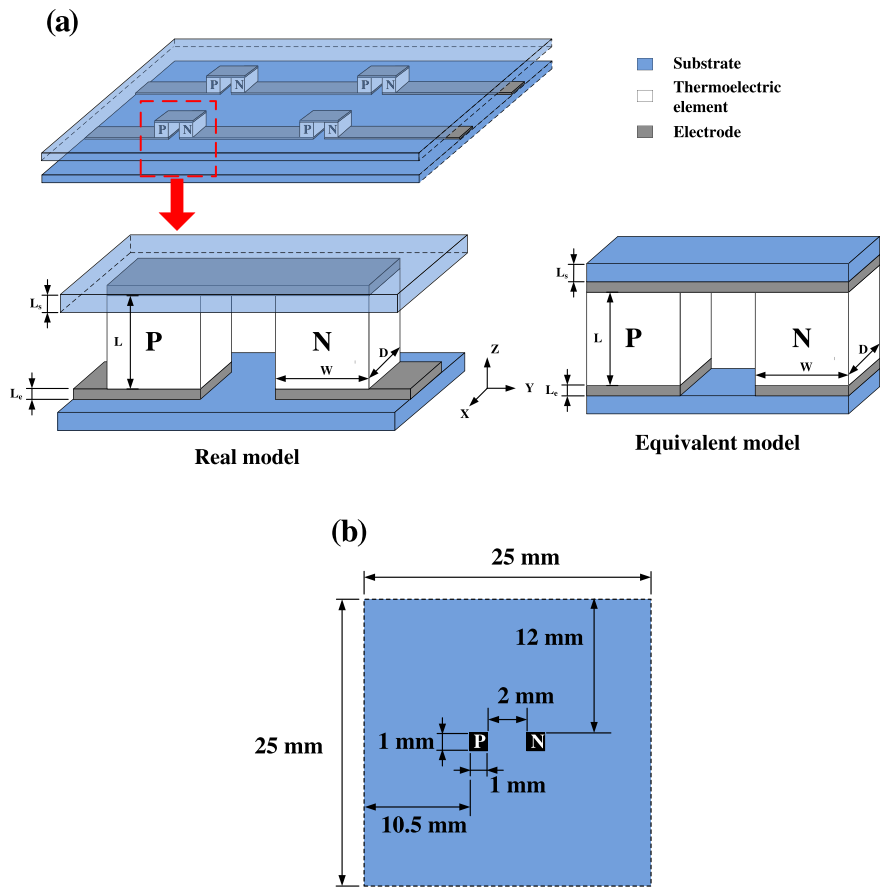


**Fig. 2.** Schematics of (a) the real model and the equivalent model and (b) the top view of a TE pair.

$$\nabla\cdot\left(\frac{1}{\rho_e}\vec{E}\right) - \nabla\cdot\left(\frac{\alpha}{\rho_e}\nabla T\right) = 0 \tag{2}$$

where $T$ and $\vec{E}$ represent the temperature and the electric field, respectively. The electric field is derived from the electric scalar potential $\phi$ ($\vec{E} = -\nabla\phi$); $\vec{J}$ represents the electric current density vector; $\alpha$, $k$, and $\rho_e$ are the Seebeck coefficient, thermal conductivity, and electrical resistivity of the thermoelectric element, respectively.

### 2.3. Boundary conditions

The boundary conditions are made up of two difference surfaces, including a hot-side surface and a cold-side surface.

#### 2.3.1. Hot-side surface

A heat flow rate $Q_{in}$ is given at the hot-side and it is obtained by [16]:

$$Q_{in} = q_s \times C_{opt} \times A_c \times \eta_{opt} \times \eta_a \times F \tag{3}$$

where $q_s$, $C_{opt}$, $A_c$, $\eta_{opt}$, $\eta_a$, and $F$ are the solar irradiance, the optical concentration ratio, the substrate area per TE pair, the optical efficiency of the Fresnel lens, the absorptance of the solar absorber, and the area factor, respectively. The optical concentration ratio is defined as the area of the lens divided by that of the solar absorber [16]. The cross-sectional area of the absorber is assumed to be equivalent to the cross-sectional area of the thermoelectric module. The area factor only exists in the case of equivalent model and it is defined as the substrate area per TE pair of the real model divided by that of the equivalent model. Additionally, the heat loss from the hot-side surface into the environment is described by heat radiation and it is expressed by

$$Q_{rd} = \varepsilon\sigma_{SB}A_cF\left(T_H^4 - T_\infty^4\right) \tag{4}$$

where $\varepsilon$, $\sigma_{SB}$, $T_H$, and $T_\infty$ are the emissivity of the solar absorber, the Stefan–Boltzmann constant ($= 5.67 \times 10^{-8}$ W m$^{-2}$ K$^{-4}$), the hot-side temperature, and the ambient temperature, respectively. In this study, the material of the solar absorber is assumed to be aluminum nitrogen cermet with the emissivity ($\varepsilon$) of 0.08 and the solar absorptance ($\eta_a$) of 0.93.

#### 2.3.2. Cold-side surface

Two different boundary conditions (Case 1 and 2) at the cold-side surface are considered. In Case 1, a constant temperature $T_L$ is given. In Case 2, the convective heat transfer is regarded and it is expressed as:

$$-k\nabla T = h_L F(T - T_\infty) \tag{5}$$

The convection heat transfer coefficient $h_L$ is assumed to be uniform at the cold-side surface. It is noted that the area factor $F$ is only given in the equivalent model.

### 2.4. Numerical method and system performance

The governing equations are discretized by a finite element scheme based on the Galerkin method [25]. Specifically, the physical scales of temperature $T$ and electric scalar potential $\phi$ over a computational element are approximated by [26]:

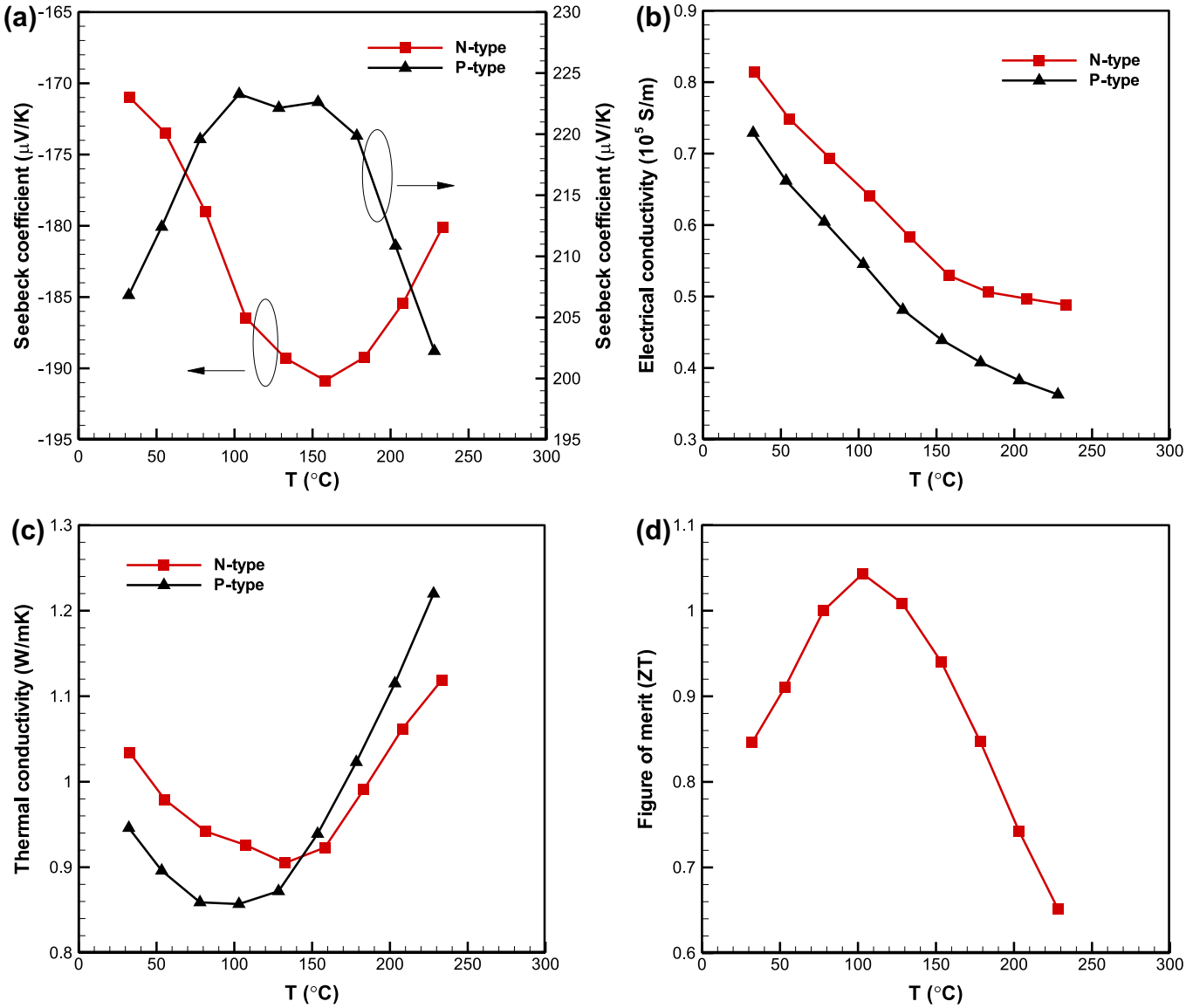


**Fig. 3.** Profiles of (a) Seebeck coefficient, (b) electrical conductivity, (c) thermal conductivity, and (d) ZT value for the solar TEG at Geometry A.

$$T = [N]\{T_e\} \tag{6}$$

$$\phi = [N]\{\varphi_e\} \tag{7}$$

where $T_e$ $\varphi_e$, and $N$ are the vector of nodal temperature, the vector of nodal electrical potentials, and the element shape function, respectively. By integrating Eqs. (1) and (2) based on the Galerkin method, the differential equations can be written as algebraic equations [26]:

$$\begin{bmatrix} K^{TT} & 0 \\ K^{\varphi T} & K^{\varphi\varphi} \end{bmatrix} \begin{Bmatrix} T_e \\ \varphi_e \end{Bmatrix} = \begin{Bmatrix} Q^L \\ I^L \end{Bmatrix} \tag{8}$$

where $Q^L$ and $I^L$ are the thermal load vector and the electric current load vector, respectively. $K^{TT}$, $K^{\varphi\varphi}$, and $K^{\varphi T}$ are the thermal stiffness matrix, the electric stiffness matrix, and the Seebeck stiffness matrix, respectively, and they are defined as [26]:

$$K^{TT} = \int_v \nabla N \cdot [k] \cdot \nabla N dV \tag{9}$$

$$K^{\varphi\varphi} = \int_v \nabla N \cdot \left[\frac{1}{\rho_e}\right] \cdot \nabla N \, dV \tag{10}$$

$$K^{\varphi T} = \int_v \nabla N \cdot \left[\frac{1}{\rho_e}\right] \cdot \left[\alpha\right] \cdot \nabla N \, dV \tag{11}$$

The three matrices and two load vectors are solved by means of the commercial software ANSYS v12.0.1. The calculations are iterated until the convergence criteria are satisfied. Convergence is defined when the relative differences of temperature and electric potential between two iterations are smaller than $10^{-6}$.

After the simulation is completed, two indexes are employed to evaluate the performance of the system. One is the output power

$P_{out}$ and the other is the total efficiency of the system $\eta_T$. The latter is expressed as [18]:

$$\eta_T = \eta_{TEG} \cdot \eta_{opt} \cdot \eta_a \tag{12}$$

where $\eta_{TEG}$ designates the conversion efficiency of the TEG which is obtained from $\eta_{TEG} = P_{out}/Q_{in}$ [18]. The material properties of the thermoelectric elements, such as the thermal conductivity, Seebeck coefficient, and electrical resistivity, are measured practically and their profiles are shown in Fig. 3. The values of the thermal conductivity and the electrical conductivity of substrate and electrode are listed in Table 1. The contact resistivity is set to be $5 \times 10^{-10}\ \Omega\ m^{-2}$ [16].

### 2.5. Analytical model of power consumption of the cooling system

The net output power of the solar TEG is evaluated by a theoretical method. The configuration of the plate-fin heat sink is sketched in Fig. 4. The flow direction of the fluid paralleling the heat sink base and the laminar and fully developed flow is assumed. Meanwhile, the fin surfaces are postulated to be isothermal due to the simplicity in theoretical analysis. Therefore, the pressure drop $\Delta p$ across the heat sink is obtained by [29]:

$$\Delta p = \frac{12\mu L_{HS} U}{D_g^2} \tag{13}$$

where $\mu$, $L_{HS}$, $U$, and $D_g$ are the fluid viscosity, the length of the heat sink, the mean velocity of the fluid, and the fin-to-fin spacing, respectively. The mean velocity is derived from the mass flow rate of fluid [29] and it is expressed by:

$$U = \frac{\dot{m}}{\rho D_g H_f n_f} \tag{14}$$

where $\dot{m}$, $\rho$, $H_f$, and $n_f$ are the mass flow rate, fluid density, fin height, and the number of fins, respectively. The mass flow rate is given by:

$$\dot{m} = \frac{Q_L}{C_p\left(T_f - T_\infty\right)} \tag{15}$$

where $Q_L$, $C_p$, $T_f$, and $T_\infty$ are the heat dissipated by the thermoelectric module at cold side, the specific heat at constant pressure, the surface temperature of fins, and the environment temperature, respectively. $Q_L$ in each simulation is solved by ANSYS. Therefore, the power consumption by the fan or pump is calculated as [29]:

$$P_{pump} = \frac{1}{\rho}\dot{m}\Delta p = \frac{12\mu L_{HS}\dot{m}^2}{\rho^2 D_g^3 H_f n_f} \tag{16}$$

The net output power is obtained by subtracting the power consumption from the output power of the solar TEG.

### 2.6. Numerical validation

By taking the temperature-dependent material properties from the study of Li et al. [16], the numerical simulation was performed

**Table 1**
Material properties and thicknesses of substrate and electrode [27,28].

| | $k$(W m$^{-1}$K$^{-1}$) | $\gamma$(S m$^{-1}$) | Thickness (mm) |
|---|---|---|---|
| Substrate ($Al_2O_3$) | 35.3 | 0 | 0.635 |
| Electrode (Cu) | 386 | $581 \times 10^5$ | 0.06 |

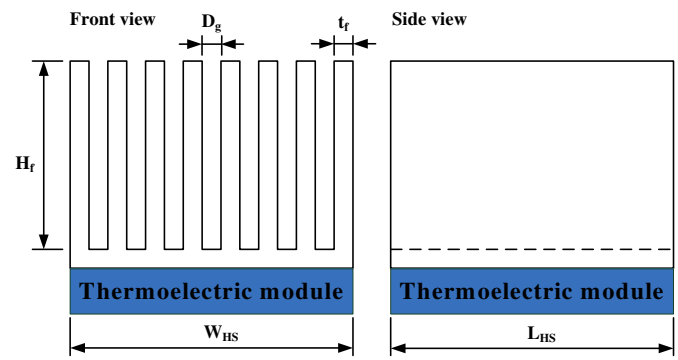


**Fig. 4.** The front view and side view of plate-fin heat sink.

at the conditions of $q_s = 900\ W\ m^{-2}$, $\eta_{opt} = 85\%$, and $T_\infty = 25\ °C$ where only one thermoelectric pair was simulated. The cross-sectional area and the length of the element were $1.3 \times 1.3\ mm^2$ and 3.9 mm, respectively. Fig. 5a suggests that the current predictions are in good agreement with the results of Li et al., thereby validating the numerical method. The numerical method was also compared to the experimental data of Kraemer et al. [20] where the thermal-concentrated solar TEG was operated at the conditions of $C_g = 1$, $C_{th} = 196$, $\eta_{opt} = 100\%$, $q_s = 1500\ W\ m^{-2}$, and $T_\infty = 20\ °C$, and the dimensions of the thermoelectric element were $1.35 \times 1.35 \times 1.65\ mm^3$. As shown in Fig. 5b, the maximum deviation between the numerical results and the experimental data is 10.5%. The deviation may be attributed to the adopted material properties from literature which were not exactly consistent the real materials and the heat loss in the experiment which was not considered in the numerical simulation. The above comparisons reveal that the developed numerical model is a feasible tool to predict the performance of the thermal-concentrated solar TEG.

## 3. Results and discussion

This study focuses on the simulation and design of a thermal-concentrated solar TEG. Three different sizes of thermoelectric element ($W$, $D$, $L$) are taken into account for comparison; they are Geometry A (1.0 mm, 1.0 mm, 1.6 mm), Geometry B (1.4 mm, 1.4 mm, 1.6 mm), and Geometry C (2.8 mm, 2.8 mm, 3.5 mm). The TEG is operated at the conditions of $C_g = 1$, $\eta_{opt} = 100\%$, $q_s = 900\ W\ m^{-2}$, and $T_\infty = 25\ °C$. The resistance of the external loading is constant in all simulations and it is assumed to be equal to that of the TE pair at 32 °C, that is, the values of the resistance at Geometry A, B, and C are 0.0416, 0.0212, and 0.0116 Ω, respectively.

### 3.1. Comparison of real model and equivalent model

The purpose of the present study is to develop an equivalent model to simplify and accelerate the simulation. Therefore, the predicted output power and total efficiency of the TEG at Geometry B based on the real model are compared to those based on the equivalent model. In Fig. 6a, the thermal concentration ratio is increased by enlarging the substrate area. It can be found that the equivalent model overestimates the performance of the TEG. When the thermal concentration ratio is low (i.e. $C_{th} \leqq 40$), the results of the equivalent model are close to those of the real model. The difference between the two models becomes obvious when the thermal concentration ratio is large to a certain extent, even though the boundary conditions between the two models are identical. The deviation between the two models stems from the thermal spreading resistance and the constriction thermal resistance

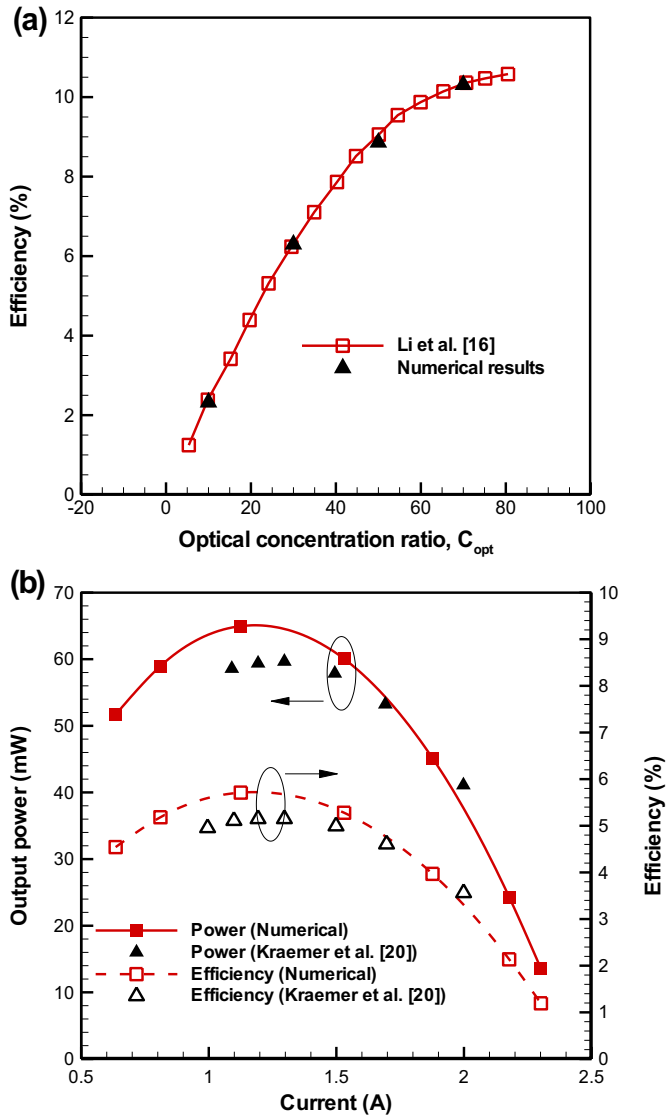


**Fig. 5.** Comparisons of (a) the efficiency of TEG and (b) the output power and efficiency of TEG.

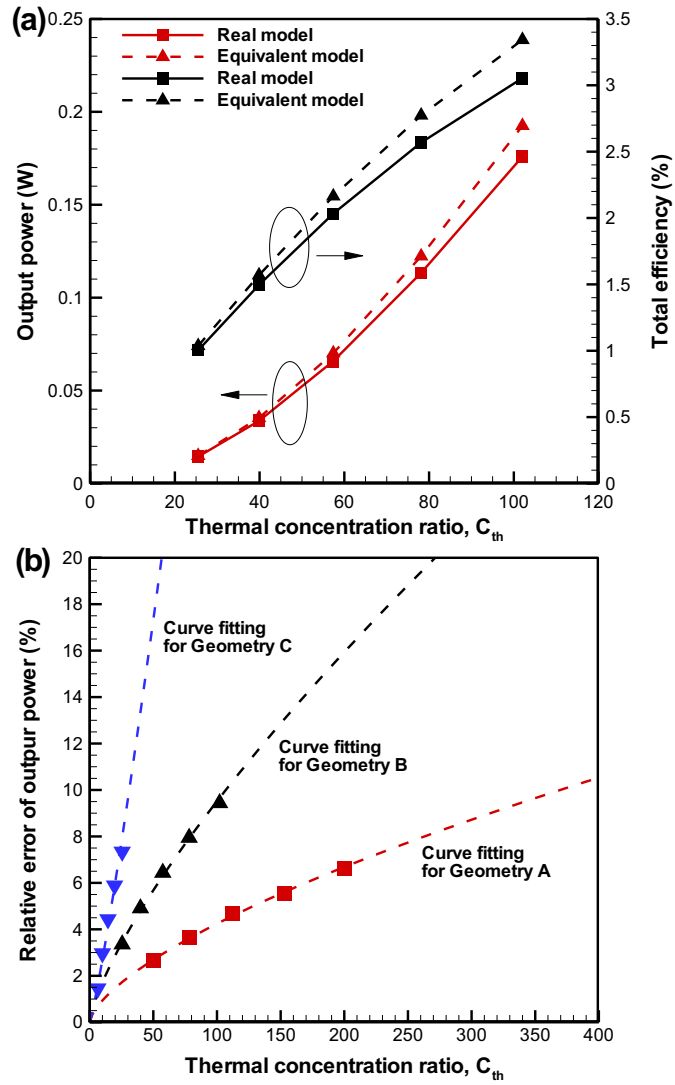


**Fig. 6.** Distributions of (a) output power and total efficiency of the TEG at Geometry B and (b) relative error of output power of the thermoelectric element sizes.

caused in the real model. When heat flows from a small area to a big one, the thermal spreading resistance is induced [12,30]. Inversely, when heat moves from a big area to a small one, the constriction thermal resistance is induced [12,30]. Because the substrate area in the equivalent model is invariant when the thermal concentration ratio varies (Fig. 2a), the realistic behavior of thermal spreading resistance and constriction thermal resistance are disregarded. This is the reason why the equivalent model overestimates the output power.

The profiles of the relative error of output power between the two models at the three geometries are shown in Fig. 6b where the relative error is defined as

$$\text{Realative error}\left(\%\right) = \frac{P_{\text{equivalent}} - P_{\text{real}}}{P_{\text{real}}} \times 100 \tag{17}$$

The deviation is ranked by Geometry C > B > A. This is because the area ratio between the substrate and the electrodes at Geometry C is larger than those at Geometries A and B. This implies, in turn, that the thermal spreading resistance and constriction thermal resistance are more significant at Geometry C [30,31]. An exponential function, $G = \exp(m\ln C_{\text{th}} + n)$, is constructed to fit the relative errors at various geometries and the fitted curves are also shown in Fig. 6b. The values of $m$ and $n$ at the three geometries are given in Table 2. Fig. 6b suggests that the established exponential function can precisely describe the relative error. Based on the established function, the predicted output power from the equivalent model is modified by

$$P = \frac{P_{\text{equivalent}}}{1 + G/100} \tag{18}$$

Following the modification, the effects of the thermal spreading resistance and the constriction thermal resistance have intrinsically

**Table 2**
Curve fitting functions ($G = e^{m\ln C_{\text{th}}+n}$) of relative error between the real model and the equivalent model.

| Geometry | A | B | C |
|---|---|---|---|
| $m$ | 0.656 | 0.744 | 1.156 |
| $n$ | −1.577 | −1.173 | −1.668 |

**Table 3**
A list of substrate area and thermal concentration ratio of three geometry types.

| Substrate type | Area ($mm^2$) | Geometry | | |
|---|---|---|---|---|
| | | A | B | C |
| | | $C_{th}$ | | |
| 1 | 40 × 40 | 50 | 25.51 | 6.38 |
| 2 | 50 × 50 | 78.13 | 39.86 | 9.96 |
| 3 | 60 × 60 | 112.5 | 57.40 | 14.35 |
| 4 | 70 × 70 | 153.13 | 78.13 | 19.53 |
| 5 | 80 × 80 | 200 | 102.04 | 25.51 |
| 6 | 90 × 90 | 253.13 | 129.15 | 32.29 |
| 7 | 100 × 100 | 312.5 | 159.44 | 39.86 |
| 8 | 110 × 110 | 378.13 | 192.92 | 48.23 |

been taken into account in the equivalent model. In other words, the disadvantage of disregarding the thermal spreading resistance and constriction thermal resistance in the equivalent model is resolved from the modified output power. After testing, the established curves of relative error can be applied for the substrate conductivity ranged from 35.3 to 130 W $m^{-1}$ $K^{-1}$. The following simulations are performed based on the equivalent model with modification.

### 3.2. Effect of substrate area or thermal concentration ratio

The effect of substrate area or thermal concentration ratio on the performance of the TEG is investigated in this section where eight different substrate areas (i.e. the substrate types 1–8) are considered, as shown in Table 3. The corresponding thermal concentration ratios of the eight substrate areas at the three geometries are given in the table as well. The substrate area of 40 × 40 $mm^2$ is a common size for commercial thermoelectric

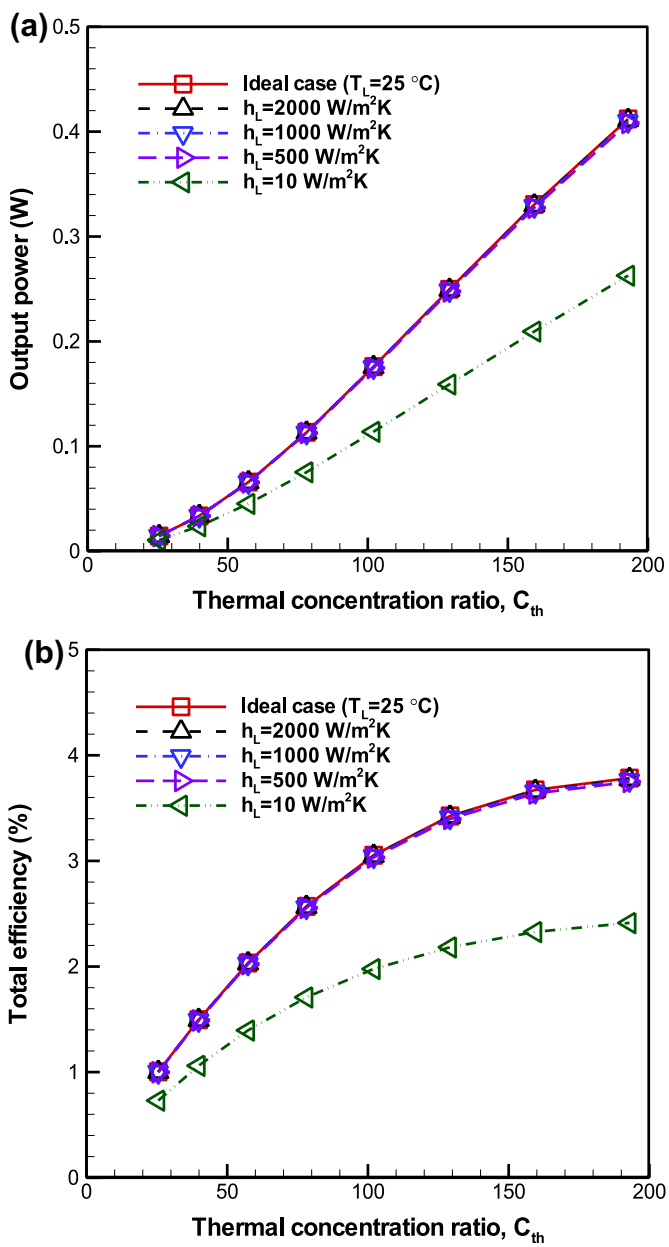


**Fig. 7.** Distributions of (a) output power and (b) total efficiency of the TEG (Geometry B) at various thermal concentration ratios and cooling conditions.

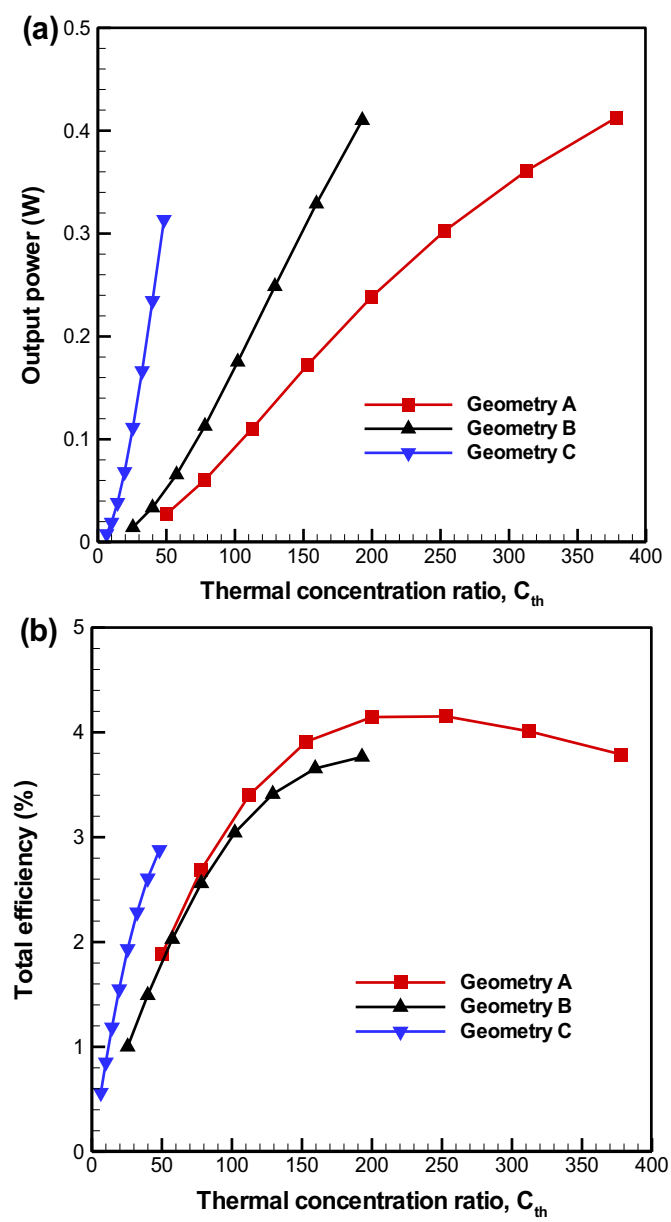


**Fig. 8.** Distributions of (a) output power and (b) total efficiency of the TEG at various thermal concentration ratios and geometries. ($h_L$ = 1000 W $m^{-2}$ $K^{-1}$).

**Table 4**
The values of $C_{th}$ and the corresponding substrate areas of three geometry types.

| Geometry | A | | B | | C | |
|---|---|---|---|---|---|---|
| $C_{th}$ | 25.51 | 39.86 | 25.51 | 39.86 | 25.51 | 39.86 |
| *Cross-sectional area of a TE pair ($mm^2$)* | 2 | | 3.92 | | 15.68 | |
| *Substrate area ($mm^2$)* | 28.57 × 28.57 | 35.71 × 35.71 | 40 × 40 | 50 × 50 | 80 × 80 | 100 × 100 |

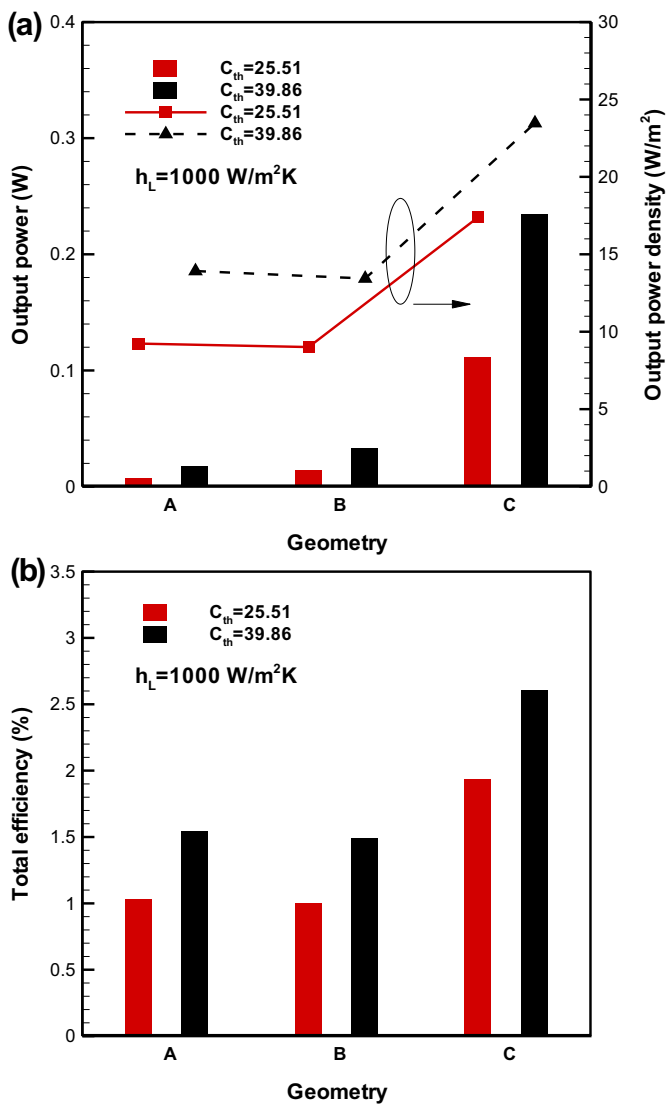


**Fig. 9.** Profiles of (a) the output power and output power density and (b) the total efficiency of the TEG. ($h_L$ = 1000 W $m^{-2}$ $K^{-1}$).

modules and it is regarded as the smallest size among the eight sizes, whereas the area of 110 × 110 $mm^2$ (slightly larger than the size demonstrated in Fig. 1b) is considered as the largest size. The distributions of the output power and total efficiency of the solar TEG at Geometry B versus thermal concentration ratio (or substrate type) are shown in Fig. 7 where four different cooling conditions or convection heat transfer coefficients are included for comparison. The output power and total efficiency increase when the thermal concentration ratio increases in all the cooling conditions. The difference among the three curves of $h_L$ = 500, 1000, and 2000 W $m^{-2}$ $K^{-1}$ is almost imperceptible, and they are very close to that of the ideal case where the convection heat transfer coefficient is assumed to be infinite. It follows that the output power of the thermal-concentrated solar TEG is independent of the convection heat transfer coefficient when the coefficient is greater than 500 W $m^{-2}$ $K^{-1}$. For the substrate type 3 ($C_{th}$ = 57.40) at $h_L$ = 500 W $m^{-2}$ $K^{-1}$, if a 1-D thermal resistance model is used to calculate the thermal resistance of the solar TEG, the ratio of the convectional thermal resistance to the total thermal resistance is around 2.0%. The ratio decreases when $h_L$ increases. This reveals that the convectional thermal resistance is by far smaller than the total thermal resistance. This is the reason why the output power is independent of the convection heat transfer coefficient when the coefficient is greater than 500 W $m^{-2}$ $K^{-1}$. The preceding characteristic is quite different from the behavior of optical-concentrated solar TEG [16] which is sensitive to the convection heat transfer coefficient. This is due to the much larger substrate area of each TE pair in the investigated TEG when compared to that in a commercial thermoelectric module. Therefore, a larger heat convection area at the cold side is obtained in the thermal-concentrated solar TEG and heat can be dissipated from the cold side to the environment more effectively. When the convection heat transfer coefficient is as low as 10 W $m^{-2}$ $K^{-1}$ which is at the condition of free convection [32], an obvious decay in the performance of the TEG is observed.

The performances of the TEG at the three geometries are presented in Fig. 8 where the convection heat transfer coefficient is 1000 W $m^{-2}$ $K^{-1}$. An increase in thermal concentration ratio monotonically increases the output power, regardless of the geometry type (Fig. 8a). Increasing thermal concentration ratio also monotonically increases the total efficiencies of the TEG at Geometries B and C, whereas there exists an optimal thermal concentration ratio or substrate area (=90 × 90 $mm^2$) at Geometry A where the maximum total efficiency of the TEG is 4.15%. This can be explained by the lower ZT value of the thermoelectric material at

**Table 5**
A list of properties of fins and coolants [32,34].

| | Fin | Coolant | |
|---|---|---|---|
| Material Property | Aluminum<br>$k_f$ = 237 W $m^{-1}$ $K^{-1}$ | Air<br>$\rho_a$ = 1.1707 kg $m^{-3}$<br>$\mu_a$ = 183.6 × $10^{-7}$ N s $m^{-2}$<br>$C_{p,a}$ = 1007 J $kg^{-1}$ $K^{-1}$ | Water<br>$\rho_w$ = 997.1 kg $m^{-3}$<br>$\mu_w$ = 891 × $10^{-6}$ N s $m^{-2}$<br>$C_{p,w}$ = 4179 J $kg^{-1}$ $K^{-1}$ |

high temperatures (Fig. 3d). The average temperature of the thermoelectric element at the substrate area of 90 × 90 mm$^2$ from the numerical prediction is about 115 °C which is close to the optimal temperature shown in Fig. 3d.

As observed in Figs. 7 and 8, the thermal concentration ratio ($C_{th}$) is an important parameter for the operation of TEG. Two values of $C_{th}$, namely, 25.51 and 39.86, are considered for comparison and the corresponding substrate areas of the three geometries are listed in Table 4. As shown in Fig. 9, the TEG at Geometry C gives the best performance among the three geometries at $C_{th}$ = 25.51 and 39.86. At a given $C_{th}$, the TEG at Geometry C has the larger substrate area than those at Geometries A and B, implying that a larger input solar energy is given in the former. It is noteworthy that the output power of the TEG at Geometry B (a larger element cross-sectional area) is slightly larger than that at Geometry A, but the power density of the former is lower than that of the latter. This behavior is consistent with the results of Jang et al. [33]. The TEGs at Geometries A and B have the same element length ($L$). The results reflect that, for a TEG at a given element length, decreasing the cross-sectional area of the thermoelectric element is a feasible route to improve the performance of the TEG, whether the substrate area or $C_{th}$ is given.

### 3.3. Effect of cooling method

The theoretical method described earlier is used to evaluate the net output power of the solar TEG, and two different coolants, air and water, are considered. The properties of the fins and coolants are listed in Table 5 [35]. It can be seen that fin-to-fin spacing ($D_g$) has the highest order in Eq. (16), so it is chosen as the operating parameter. The height ($H_f$) and thickness ($t_f$) of the fins are 14 mm and 0.2 mm, respectively [24]. The base area of the heat sink is assumed to be equal to the substrate area of the thermoelectric module, so the width ($W_{HS}$) and the length ($L_{HS}$) of the sink are decided by the given substrate area. The distribution of the power

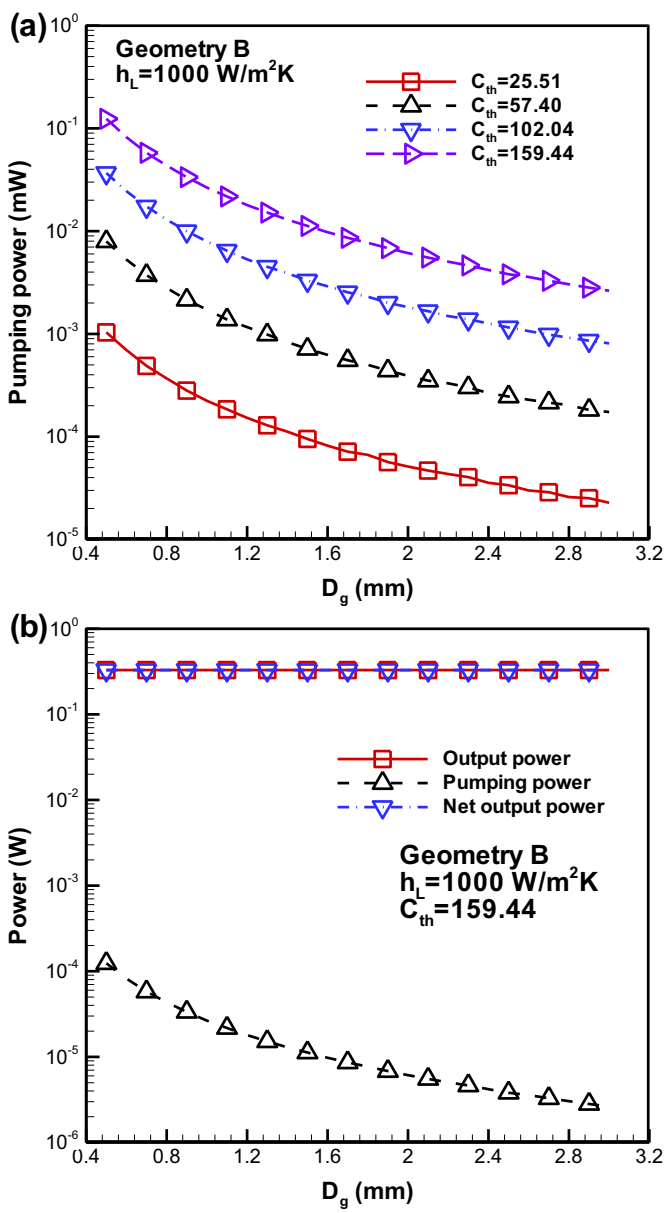


**Fig. 10.** Distributions of (a) pumping power for water cooling and (b) the power of the TEG at Geometry B.

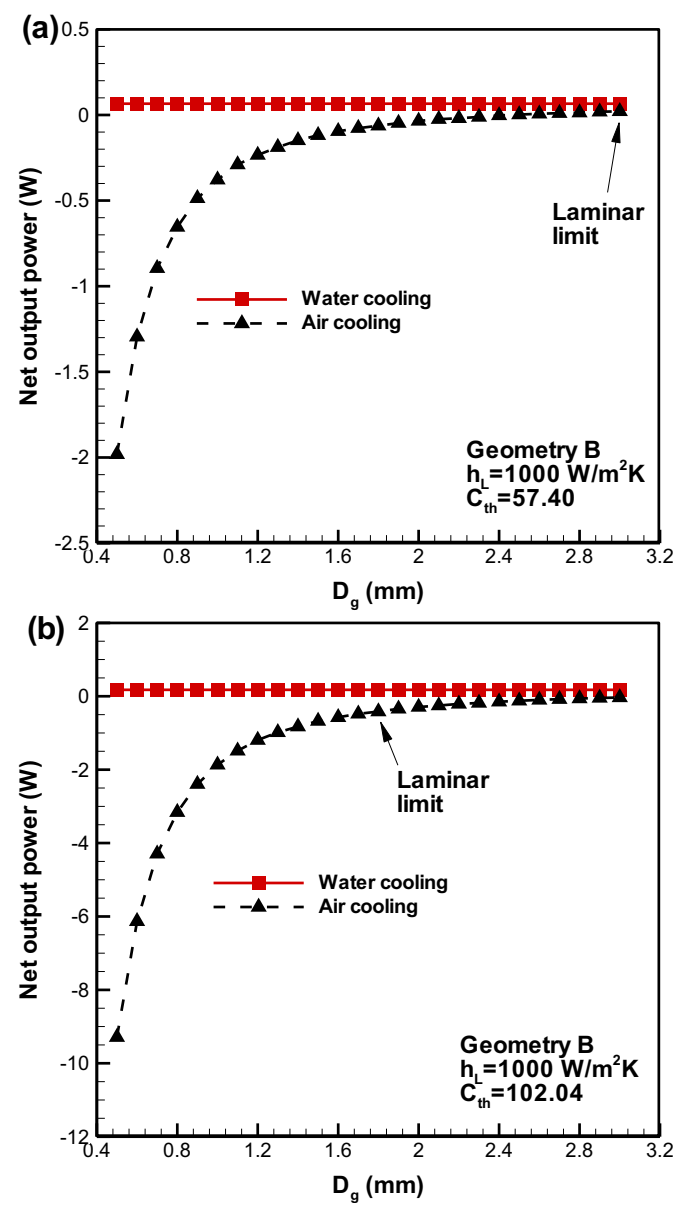


**Fig. 11.** Distributions of net output power of the solar TEG at Geometry B at $C_{th}$ = (a) 57.40 and (b) 102.04.

for the TEG at Geometry B is shown in Fig. 10 where the water cooling is carried out. Fig. 10a shows that the pumping power decreases when $D_g$ increases or $C_{th}$ decreases. Fig. 10b suggests that the required pumping power is substantially smaller than that of the output power of the TEG within the investigated range of $D_g$ ($C_{th} = 159.44$). Consequently, the net output power is almost invariant with varying $D_g$ when water cooling is adopted. The comparisons of net output power between water cooling and air cooling at $C_{th} = 57.40$ and 102.04 are shown in Fig. 11. With the condition of $C_{th} = 57.40$ and under the same cooling condition ($h_L = 1000\ \mathrm{W\ m^{-2}\ K^{-1}}$), a negative net output power is obtained for air cooling when a small $D_g$ is used. The positive net output power for air cooling can be obtained only when $D_g$ is large enough (Fig. 11a). However, when $C_{th}$ is 102.04, the positive net output power under air cooling cannot be obtained in the investigated range of $D_g$ (Fig. 11b). Additionally, the Reynolds number will exceed the laminar limit (2300) [35] if $D_g$ is too large (the limit value of $D_g$ becomes smaller when $C_{th}$ increases as shown in Fig. 11b), which doesn't take place for water cooling. Accordingly, water cooling is a better cooling method to maximize the net output power of the solar TEG, stemming from the larger specific heat of water.

## 4. Conclusions

The performance of a thermal-concentrated solar TEG has been investigated using a numerical method where the temperature-dependent properties of the commercial thermoelectric material were taken into account. In the method, an equivalent model was developed to simulate the real-sized TEG module and an analytical method was used to evaluate the power consumption for cooling the TEG module. By introducing an exponential function with the consideration of the constriction thermal resistance and thermal spreading resistance in the equivalent model, numerical simulations with much less computational time was achieved.

Three different geometry types (Geometries A, B, and C) of TEG were tested and compared with each other. The predictions suggest that the output power of the solar TEG increases with increasing substrate area, stemming from the increased thermal concentration ratio. The smallest element (Geometry A) gives the best performance and the maximum efficiency is 4.15% when the substrate area is $90 \times 90\ \mathrm{mm}^2$, as a consequence of lower $ZT$ value of the thermoelectric materials at high temperatures. When the element length is fixed, decreasing the cross-sectional area of the thermoelectric element is a better route to improve the performance. The cooling conditions almost play no part in the performance of the solar TEG when the forced convection with the conditions of $h_L \geqq 500\ \mathrm{W\ m^{-2}\ K^{-1}}$ is encountered. According to the theoretical method, a larger and positive net output power can be achieved using water cooling for the solar TEG. This work has provided a useful insight into the design of practical thermal-concentrated solar TEG system.

## Acknowledgments

The authors acknowledge the financial support from Bureau of Energy, Ministry of Economic Affairs, Taiwan, ROC, for this study.

## References

[1] Wang XT, Huang YX, Cheng CH, Lin DTW, Kang CH. A three-dimensional numerical modeling of thermoelectric device with consideration of coupling of temperature field and electric potential field. Energy 2012;47:488–97.
[2] Gou X, Yang S, Xiao H, Ou Q. A dynamic model for thermoelectric generator applied in waste heat recovery. Energy 2013;52:201–9.
[3] Bell LE. Cooling, heating, generating power, and recovering waste heat with thermoelectric systems. Science 2008;321:1457–61.
[4] Martínez A, Astrain D, Rodríguez A. Dynamic model for simulation of thermoelectric self cooling applications. Energy 2013;55:1114–26.
[5] Simons RE, Ellsworth MJ, Chu RC. An assessment of module cooling enhancement with thermoelectric coolers. J Heat Transfer Trans ASME 2005;127:76–84.
[6] Maneewan S, Chindaruksa S. Thermoelectric power generation system using waste heat from biomass drying. J Electron Mater 2009;38:974–80.
[7] Gou X, Xiao H, Yang S. Modeling, experimental study and optimization on low-temperature waste heat thermoelectric generator system. Appl Energy 2010;87:3131–6.
[8] Sahin AZ, Yilbas BS, Shuja SZ, Momin O. Investigation into topping cycle: thermal efficiency with and without presence of thermoelectric generator. Energy 2011;36:4048–54.
[9] Chen WH, Syu YJ. Thermal behavior and hydrogen production of methanol autothermal reforming with spiral preheating. Int J Hydrogen Energy 2011;36:3397–408.
[10] Chen WH, Chung YC, Liu JL. Analysis on energy consumption and performance of reheating furnaces in a hot strip mill. Int Commun Heat Mass Transfer 2005;32:695–706.
[11] Rowe DM. Thermoelectric waste heat recovery as a renewable energy source. Int J Innov Energy Syst Power 2006;1:13–23.
[12] Hsiao YY, Chang WC, Chen SL. A mathematic model of thermoelectric module with applications on waste heat recovery from automobile engine. Energy 2010;35:1447–54.
[13] Hsu CT, Huang GY, Chu HS, Yu B, Yao DJ. Experiments and simulations on low-temperature waste heat harvesting system by thermoelectric power generators. Appl Energy 2011;88:1291–7.
[14] Chen WH, Liao CY, Hung CI, Haung WL. Experimental study on thermoelectric modules for power generation at various operating conditions. Energy 2012;45:874–81.
[15] Mekhilef S, Saidur R, Safari A. A review on solar energy use in industries. Renew Sustain Energy Rev 2011;15:1777–90.
[16] Li P, Cai L, Zhai P, Tang X, Zhang Q, Niino M. Design of a concentration solar thermoelectric generator. J Electron Mater 2010;39:1522–30.
[17] Fan H, Singh R, Akbarzadeh A. Electric power generation from thermoelectric cells using a solar dish concentrator. J Electron Mater 2011;40:1311–20.
[18] Yang T, Xiao J, Li P, Zhai P, Zhang Q. Simulation and optimization for system integration of a solar thermoelectric device. J Electron Mater 2011;40:967–73.
[19] Xiao J, Yang T, Li P, Zhai P, Zhang Q. Thermal design and management for performance optimization of solar thermoelectric generator. Appl Energy 2012;93:33–8.
[20] Kraemer D, Poudel B, Feng HP, Caylor JC, Yu B, Yan X, et al. High-performance flat-panel solar thermoelectric generators with high thermal concentration. Nat Mater 2011;10:532–8.
[21] Chen G. Theoretical efficiency of solar thermoelectric energy generators. J Appl Phys 2011;109:104908.
[22] Zebarjadi M, Esfarjani K, Dresselhaus MS, Ren ZF, Chen G. Perspectives on thermoelectrics; from fundamentals to device applications. Energy Environ Sci 2012;5:5147–62.
[23] Chen WH, Liao CY, Hung CI. A numerical study on the performance of miniature thermoelectric cooler affected by Thomson effect. Appl Energy 2012;89:464–73.
[24] Wang CC, Hung CI, Chen WH. Design of heat sink for improving the performance of thermoelectric generator using two-stage optimization. Energy 2012;39:236–45.
[25] Moaveni S. Finite element analysis: theory and applications with ANSYS. 2nd ed. New Jersey: Prentice Hall; 2003.
[26] Antonova EE, Looman DC. Finite elements for thermoelectric device analysis in ANSYS. In: 24th Int conference on thermoelectrics 2005. p. 200.
[27] Meng F, Chen L, Sun F. A numerical model and comparative investigation of a thermoelectric generator with multi-irreversibilities. Energy 2011;36:3513–22.
[28] Pérez-Aparicio JL, Palma R, Taylor RL. Finite element analysis and material sensitivity of Peltier thermoelectric cells coolers. Int J Heat Mass Transfer 2012;55:1363–74.
[29] Mereu S, Sciubba E, Bejan A. The optimal cooling of a stack of heat generating boards with fixed pressure drop, flowrate or pumping power. Int J Heat Mass Transfer 1993;36:3677–86.
[30] Lee S, Song S, Au V, Moran KP. Constriction/spreading resistance model for electronic packing. ASME/JSME Therm Eng Conf 1995;4:199–206.
[31] Chen YS, Chien KH, Wang CC, Hung TC, Ferng YM, Pei BS. Investigations of the thermal spreading effects of rectangular conduction plates and vapor chamber. J Electron Package 2007;129:348–55.
[32] Incropera FP, Dewitt DP, Bergman TL, Lavine AS. Fundamentals of heat and mass transfer, Hoboken. 6th ed. John Wiley & Sons; 2007.
[33] Jang B, Han S, Kim JY. Optimal design for micro-thermoelectric generators using finite element analysis. Microelectron Eng 2011;88:775–8.
[34] Bejan A. Convection heat transfer. 2nd ed. New York: John Wiley & Sons; 1995.
[35] Copeland D. Optimization of parallel plate heatsinks for forced convection. In: Proc of the 16th IEEE semi-therm symposium 2000. p. 266–72.